Journal of Quantitative Spectroscopy & Radiative Transfer 100 (2006) 429–436

Journal of Quantitative Spectroscopy & Radiative Transfer

www.elsevier.com/locate/jqsrt

Scattering matrices and reflectance spectra of forsterite particles with different size distributions

H. Volten[a,*], O. Muñoz[b], J.R. Brucato[c], J.W. Hovenier[a], L. Colangeli[c], L.B.F.M. Waters[a,d], W.J. van der Zande[e]

[a]*Astronomical Institute "Anton Pannekoek", University of Amsterdam, Kruislaan 403, 1098 SJ Amsterdam, The Netherlands*
[b]*Instituto de Astrofísica de Andalucía, CSIC, Camino Bajo de Huétor 50, Granada 18008, Spain*
[c]*INAF - Osservatorio Astronomico di Capodimonte, via Moiariello 16, 80131 Napoli, Italy*
[d]*Instituut voor Sterrenkunde, Katholieke Universiteit Leuven, Celestijnenlaan 200B, B-3001 Heverlee, België*
[e]*Institute for Molecules and Materials, Radboud University Nijmegen, PO Box 9010, NL-6500 GL Nijmegen, The Netherlands*

Abstract

We present measurements of the complete scattering matrix as a function of the scattering angle of three different samples of forsterite particles in random orientation at a wavelength of 632.8 nm. The three samples were prepared so that three different size distributions were obtained. The composition and reflection spectra of the three samples have been experimentally determined. The results indicate that the elements of the scattering matrix are affected in a different way by the size differences. Since light scattering by comets is probably caused by particles similar to our forsterite particles, the results potentially contain information on the size of the cometary particles.

Keywords: Scattering; Polarization; Comets; Dust; Forsterite

1. Introduction

The physical properties of crystalline forsterite particles are of key importance to interpret observations in many different astronomical environments, such as comets [1–5], interplanetary dust [6], and disks around stars [7–10]. The irregularity in grain shape strongly affects their scattering properties, including polarization and their spectral behavior. Numerical techniques alone are not adequate to efficiently simulate these properties. Therefore, experiments are essential.

Not only the shapes but also the particle sizes are of crucial importance. The size distribution is affected by large uncertainties, e.g., in cometary research [11,12], but we need to know it for inferring other properties, such as the mass of the dust released from the cometary nucleus. Therefore, it is of main importance to know how differences in the size distribution of cometary dust can affect their scattering behavior.

*Corresponding author. Tel.: +31 205257491; fax: +31 205257484.
E-mail address: hvolten@science.uva.nl (H. Volten).

0022-4073/$ - see front matter
doi:10.1016/j.jqsrt.2005.11.074

In this work, we study three samples of forsterite (Mg-rich olivine) particles. The samples have been obtained from the same bulk sample, i.e. they all have the same composition and crystal structure, and therefore similar particle shapes, but different size distributions. This study is part of an ongoing project to distinguish the size from the composition and shape effects on the scattering behavior [13]. We have measured the complete scattering matrices (including polarization) as a function of the scattering angle of the three samples of particles in random orientation. The measurements have been performed at a wavelength of 632.8 nm.

In Section 2 we give a detailed description of the physical properties of our samples, i.e., particle shapes, size distributions, chemical composition, and diffuse reflectance spectra from the ultraviolet to the mid infrared. In Section 3 we present a brief description of the experimental equipment used to measure the scattering matrices of our samples. The measurements and discussion are presented in Section 4.

2. Sample characterization

Olivine is a magnesium-iron silicate $(Mg, Fe)_2SiO_4$. It occurs in a continuous range of magnesium and iron ratio compositions between pure magnesium silicate (forsterite Mg_2SiO_4) and pure iron silicate (fayalite Fe_2SiO_4). What we call forsterite samples in this work are samples consisting of magnesium-rich olivine particles with a stochiometric composition of $Mg_{1.9}Fe_{0.1}SiO_4$, i.e. 95% pure forsterite, collected in North Carolina, USA.

2.1. Size distributions and morphology

The bulk forsterite sample was first ground with an Agatha ball miller. Subsequently, we produced samples with three different size distributions by using dry and wet sieving. To give an impression of the shapes of the particles we show in Fig. 1 field emission scanning electron microscopy (FESEM) images of the three forsterite samples studied in this work. The FESEM images were obtained by using a Cambridge Model FESEM microscope (Stereoscan 360FE). As shown in Fig. 1, the forsterite particles have irregular shapes with very sharp edges. The bulk sample has been dry sieved first with a 50 μm sieve and then with a 20 μm sieve. In principle, particles remaining on the 20 μm sieve should have diameters between 20 and 50 μm. By dry sieving, however, we could not remove all particles with diameters smaller than 20 μm. Small particles remained stuck on the surface of the larger particles due to electrostatic forces (Fig. 1, top panel). This sample is designated as sample *Finitial*. Subsequently, wet sieving was used to produce a sample with particles in the 20–50 μm diameter range (*Fwashed*). In this case the sieving procedure was carried out in pure ethanol. In this way, the finest particles were removed from the original sample (see Fig. 1, middle panel). These small grains were then collected and dried to constitute sample *Fsmall* (Fig. 1, bottom panel).

The projected surface area distributions, $S(\log r)$, were measured by using a Fritsch laser particle sizer. The particle sizer is based on diffraction without making assumptions about the refractive indices of the materials of the particles [14,15]. In Fig. 2 we present $S(\log r)$ as a function of $\log r$ with r in μm for the three forsterite samples studied in this work. Here, $S(\log r)\,\mathrm{d}\log r$ is the relative contribution by projected-surface-equivalent spheres with radii in the size range $\log r$ to $\log r + \mathrm{d}\log r$ to the total projected surface per unit volume of space. The plotted curves are normalized in such a way that the area under a curve yields one. Notwithstanding the elaborate sieving procedure, the three resulting projected surface area distributions are still remarkably similar for sizes smaller than about 1 μm (see Fig. 2). The sieving method seems to work best for particles larger than a few micrometers in equivalent radius. In fact, Fig. 2 shows that for r larger than about 10 μm, $S(\log r)$ is largest for the *Fwashed* sample, but *Fsmall* does not totally vanish there. In Fig. 2 we also present the effective radius, r_{eff}, and the effective variance, v_{eff}, as defined by Hansen and Travis [16].

In cometary research, the normalized number distribution $n(r)$ as a function of r is often used. Our measured $S(\log r)$, can be transformed into such a number distributions by using the relation

$$S(\log r) = Cr^3 n(r), \tag{1}$$

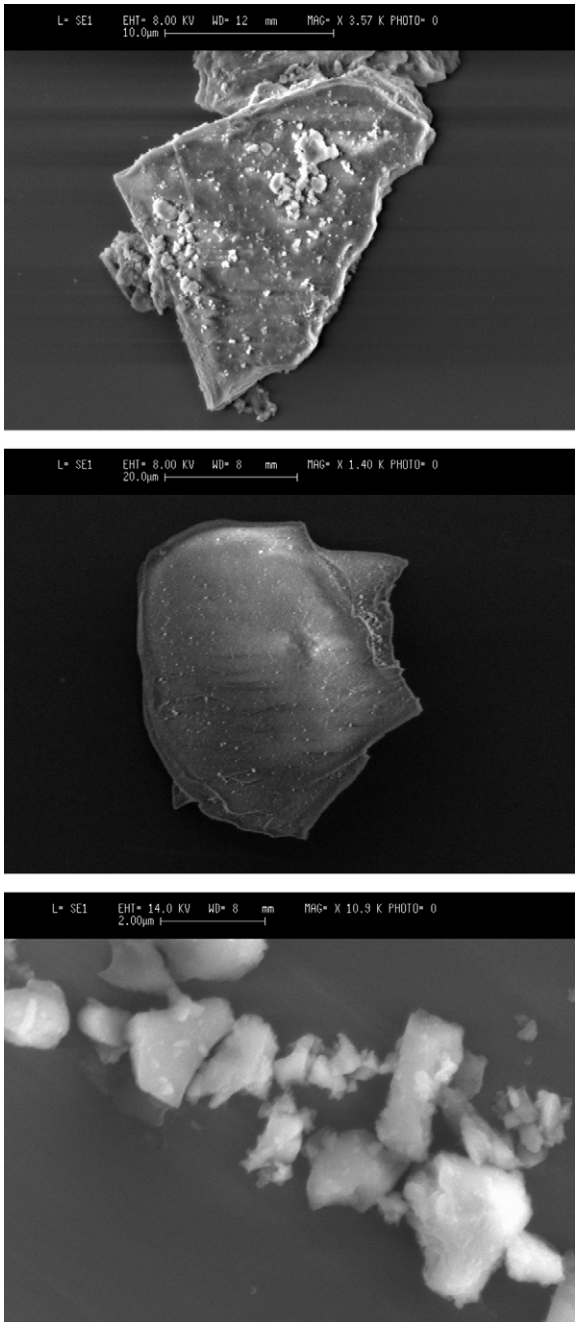

Fig. 1. Field emission scanning electron microscope (FESEM) images of the three forsterite samples: *Finitial* (top panel), *Fwashed* (middle panel), and *Fsmall* (bottom panel). White bars at the upper part of each image denote the scale. Note that FESEM images are not suited to infer representative information on the size of the particles.

where C is a constant determined by the normalization procedure used, i.e.

$$C = \int_0^\infty \frac{S(\log r)}{r^3}\,\mathrm{d}r. \tag{2}$$

For more detailed information on size distributions and on how to transform one type into the other we refer to Volten et al. [17] and the website at www.astro.uva.nl/scatter

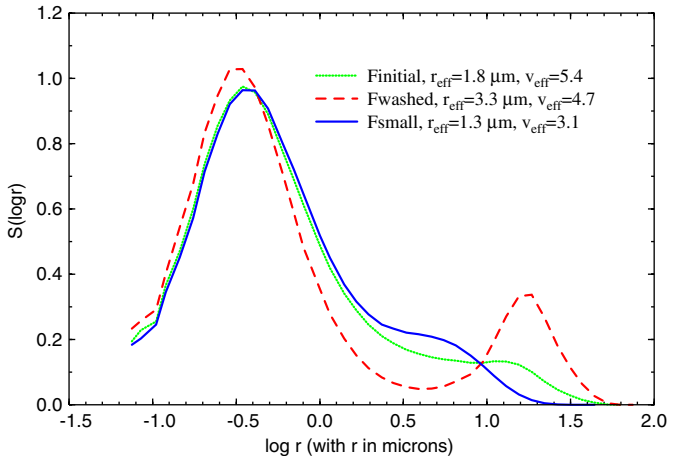

Fig. 2. Normalized projected-surface-area distributions as a function of $\log r$. The r_{eff} and v_{eff} for the three samples are also given.

Table 1
EDX analysis results for the forsterite samples

Composition	*Finitial*	*Fwashed*	*Fsmall*
MgO	50.5 ± 0.8	52 ± 2	50.4 ± 1.2
SiO_2	36.6 ± 0.7	37.1 ± 1.0	36.9 ± 1.2
FeO	7.4 ± 0.4	7.7 ± 0.3	7.5 ± 0.4
NiO	0.42 ± 0.18	0.42 ± 0.11	0.47 ± 0.11

The four main components are given in mass %.

2.2. Elemental composition and refractive indices

In Table 1 we list the energy dispersive X-ray (EDX) analysis results for the three analyzed samples. Each value is the average of about 20 measurements of different places of the sample. As shown in Table 1, the composition of the three forsterite samples is identical (within the error bars). Therefore, we also expect their refractive indices to be identical. The exact values of the refractive indices of our samples are unknown. According to the measured optical constants of different types of silicate particles listed in the Jena-St. Petersburg database (http://www.astro.spbu.ru/JPDOC/ [18]), we estimate the real part of the refractive index to be around 1.63 and the imaginary part to be around 10^{-5}.

2.3. Diffuse reflectance spectra

We obtained diffuse reflectance spectra of the three samples from 0.2 to 25 µm by using two types of laboratory equipment. We used a Fourier transform Michelson interferometer (Bruker, Model Equinox 55) in the mid infrared from 1.25 to 25 µm and a Perkin-Elmer Lambda 19 spectrometer in the ultraviolet-visible-near infrared from 0.2 to 2.5 µm. The overlapping region in the near infrared was used to merge the spectra. To perform spectroscopic measurements in reflectance, the samples were gently settled into a cup-shaped sample holder avoiding grain packing. In the mid-infrared spectral region we used an optical accessory Graseby Specac Model Selector with a biconical geometric configuration [19] and acquired a spectral resolution of $2\,\text{cm}^{-1}$. In order to compensate for instrumental features and for atmospheric H_2O and CO_2 background, we performed before each forsterite measurement a reference measurement of KBr dust, that has no features in the covered wavelength range.

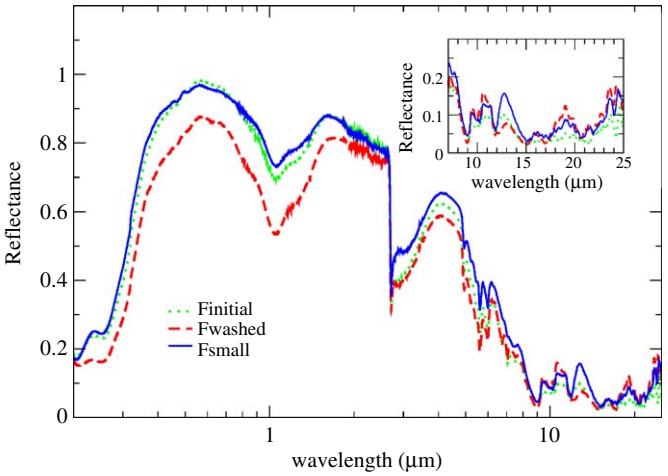

Fig. 3. Reflectance spectra in percentage of incident light as a function of wavelength. The inset shows on a linear scale the range in which the reststrahlen bands are situated.

In the ultraviolet-visible-near infrared spectral region we used an integrating sphere (Labsphere) coated inside with Halon/Spectralon to acquire the directional hemispherical diffuse reflectance spectra. The spectral resolution was 3 nm and a Halon/Spectralon standard was used in order to obtain the background reference spectra.

The reflectance measurements obtained in the two spectral regions for the three *Finitial*, *Fwashed*, and *Fsmall* forsterite samples overlapped perfectly in the near-infrared. The merged spectra are reported in Fig. 3. In the overall spectral range an expected dependence of the diffuse reflectance on the grain sizes is observed. At wavelengths smaller than 0.7 μm, which includes the wavelength at which we performed the scattering measurements, the diffuse reflectance of *Fsmall* is about 10% higher than that of the *Fwashed* sample, but it is similar to the diffuse reflectance of *Finitial*. This indicates that the diffuse reflectance at these wavelengths is dominated by small grains. The near infrared olivine band is centered at 1.05 μm and the line position is the same for all samples. The fundamental reststrahlen bands peak at 9.47, 10.10, 10.55, 16.00, 18.90, 23.53 and 24.21 μm. As a rule, the strength of these spectral features decreases with decreasing particle size. Indeed, the reflectance in the reststrahlen bands of *Fwashed* lies above the *Fsmall* curve. *Finitial* does not seem to follow this rule since its curve lies under the others. However, the *Finitial* sample has a larger effective variance than the samples *Fwashed* and *Fsmall* (see Fig. 2). For this reason this simple rule may not apply. In contrast, we see that the strength of the feature at 12.74 μm increases when the small particles dominate. The features present in the spectral region 4.76–7.14 μm are attributed to overtones or combination modes and the feature at about 2.9 μm is due to water molecules adsorbed on forsterite grains.

3. Light scattering experiments

In this section we give a brief review of some basic scattering concepts and a description of our light scattering experiments. For a more detailed description we refer to Hovenier [20], and Hovenier et al. [21].

The intensity and state of polarization of a beam of light can be described by means of the Stokes vector, **I**. The scattering matrix **F**, of an ensemble of particles describes how the Stokes vector of the incident beam is transformed into the Stokes vector of the scattered beam (apart from a multiplicative constant). The scattering matrix is defined as follows: if the Stokes vector of an incident beam, is multiplied by **F** we obtain a scalar times the Stokes vector of the (once) scattered light, which, for randomly oriented particles, is sufficiently described by means of the scattering angle, θ. Moreover, if we deal with randomly oriented particles and their mirror particles are present in equal numbers the scattering matrix has the

simple form

$$\mathbf{F}(\theta) = \begin{pmatrix} F_{11}(\theta) & F_{12}(\theta) & 0 & 0 \\ F_{12}(\theta) & F_{22}(\theta) & 0 & 0 \\ 0 & 0 & F_{33}(\theta) & F_{34}(\theta) \\ 0 & 0 & -F_{34}(\theta) & F_{44}(\theta) \end{pmatrix}. \tag{3}$$

Experiments for similar samples have demonstrated that this form is correct to a high degree of approximation [21]. Therefore,

$$\mathbf{I_{sca}} \propto \mathbf{F}(\theta)\mathbf{I_{inc}}, \tag{4}$$

where, $\mathbf{I_{inc}}$ and $\mathbf{I_{sca}}$ are the Stokes vectors of the incident and scattered light, respectively.

In Eq. (3) $F_{11}(\theta)$ is proportional to the phase function or the scattering function and $-F_{12}(\theta)/F_{11}(\theta)$ is the degree of linear polarization for unpolarized incident light.

In our experimental apparatus we use a HeNe laser (632.8 nm, 5 mW) as light source. The laser light in our experiments passes through a polarizer and an electro-optic modulator. The modulated light is subsequently scattered by an ensemble of randomly oriented particles taken from the sample located in a jet stream produced by an aerosol generator. In this way, the scattering matrix can be determined by measuring the Stokes vectors of the scattered light for various Stokes vectors of the incident light. The particles of a particular sample are brought into the jet stream as follows. A compacted mass of powder is loaded into a cylindrical feed stock reservoir. A piston pushes the powder onto a rotating brush at a certain speed. An air stream carries the aerosol particles of the brush through a tube to a nozzle above the scattering volume. The scattered light may pass through a quarter-wave plate and an analyzer (both optional) and is then detected by a photomultiplier tube which moves in steps along a ring around the ensemble of particles. In this way a range of scattering angles is covered from 5° (nearly forward scattering) to 173° (nearly backward scattering). We normalize all measured phase functions to 1 at 30°. All matrix elements (except F_{11} itself) are divided by F_{11}, that is, we consider F_{ij}/F_{11}, with $i,j = 1$–4 with the exception of $i = j = 1$. Another photomultiplier is placed at a fixed position and used to correct for fluctuations in the particle stream. For all measurements reported in this paper, we have investigated the reliability of the measured scattering matrices by checking that they satisfy the Cloude test [22] for each scattering angle.

4. Scattering matrices and discussion

In Fig. 4 we present the measured scattering matrix elements as functions of the scattering angle for the *Finitial*, *Fwashed*, and *Fsmall* forsterite samples. The experimental errors are indicated by error bars. When no error bar is shown the value for the standard deviation of the mean value is smaller than the symbol plotted. The scattering matrix elements for the three forsterite samples follow the general trends presented by irregular compact mineral particles (see e.g. [23,24]). The measured phase functions have a strong forward peak and vary little at side and backscattering angles. The measured $F_{44}(\theta)/F_{11}(\theta)$ for our forsterite irregular particles is larger than $F_{33}(\theta)/F_{11}(\theta)$ for angles larger than about 80°. Moreover, $F_{22}(\theta) \neq F_{11}(\theta)$ at all scattering angles, which is another indication of the nonsphericity of our particles since for spherical particles these two elements are equal to each other at all scattering angles.

The measured $-F_{12}(\theta)/F_{11}(\theta)$ curves show the typical bell shape found for irregular mineral particles. The degree of linear polarization for unpolarized incident light for the three forsterite samples takes on negative values at scattering angles larger than ~150°. The minima lie around 160°–165° with values varying between −3.7% for the *Finitial* sample and −2.4% for the *Fwashed* sample. The maximum polarization varies between 18% and 21% at $\theta = 90°-95°$.

Despite the similarity of the scattering matrices for the three forsterite samples, we still see significant differences. These must be mostly due to the small differences in the size distributions since the other physical parameters (i.e., refractive indices and shapes) are very similar for the three samples (see Section 2). The differences in sizes between the three samples affect different scattering matrix elements in a different way. For instance, $F_{22}(\theta)/F_{11}(\theta)$ for the *Fwashed* and *Finitial* samples are practically identical at almost all scattering

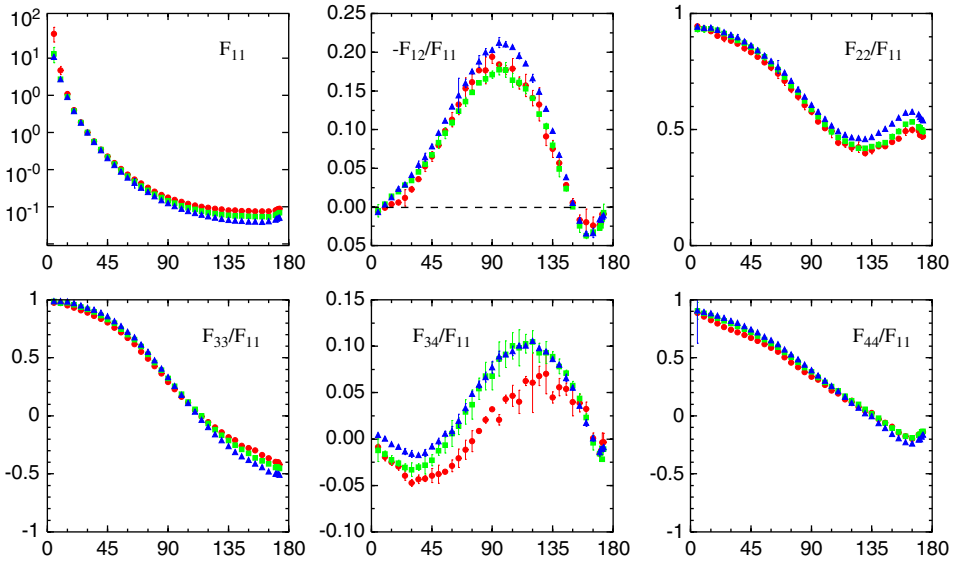

Fig. 4. Measured scattering matrix elements as a function of the scattering angle for *Finitial* (squares), *Fwashed* (circles), and *Fsmall* (triangles).

angles, despite the considerable difference in size distribution in the micron-size range, whereas the measurements for the *Fsmall* sample present higher values especially in the 100°–173° angle range. In contrast, the $F_{34}(\theta)/F_{11}(\theta)$ ratio for *Fwashed* is clearly different from that of *Finitial* and *Fsmall* as might indeed be expected from the similarity between these samples as shown in Figs. 2 and 3. Again like the $F_{22}(\theta)/F_{11}(\theta)$ ratio, the measured degree of linear polarization for unpolarized incident light, i.e. $-F_{12}(\theta)/F_{11}(\theta)$, of the *Fsmall* sample stands out: it shows the highest maximum. It is interesting to note that the negative branch of the $-F_{12}(\theta)/F_{11}(\theta)$ ratio located at angles larger ~150°, also shows differences for the three samples studied. Here, the lowest values are obtained for samples *Finitial* and *Fsmall*, but the *Fwashed* sample, shows higher values in the same angle range.

5. Conclusions

The three forsterite samples form an interesting set since they are virtually identical in all respects except for their size distributions. These differ in particular in the particle size range larger than a few micrometers. Effects of these size differences also show up in the reflection spectra. For the scattering matrix elements the most striking effects are found for the ratios $-F_{12}(\theta)/F_{11}(\theta)$ and $F_{22}(\theta)/F_{11}(\theta)$, where the sample with the smallest r_{eff}, i.e. *Fsmall*, stands out the most, and $F_{34}(\theta)/F_{11}(\theta)$ where it is the sample with the largest r_{eff}, i.e. *Fwashed*, that behaves differently from the other two.

The bell shape of the measured polarization scattering curves, $-F_{12}(\theta)/F_{11}(\theta)$, is similar to that observed for comets in the 0.3 to 2.2 μm wavelength range (see e.g. [25–28]). All observed comets have nearly identical polarization scattering (or phase) curves for scattering angles larger than ~140°. They have a negative branch at scattering angles larger than 150°–160° with a minimum of about 2% around 170°. The main differences between observed comets concern the maximum in positive polarization that varies between 10% and 30% at $\theta = 80°-90°$. If the behavior of the polarization curve of comets is indeed to a large extent caused by scattering of particles similar to our forsterite particles, the height of the polarization maximum and the depth of the negative branch potentially contain information on the size of the cometary particles.

Acknowledgements

The work of O. Muñoz has been partially supported by contracts AYA2004-03250 and ESP2003-00357. We are grateful to Martin Konert of the Free University in Amsterdam for measuring the size distributions.

References

[1] Crovisier J, Leech K, Bockelee-Morvan D, Brooke TY, Hanner MS, Altieri B, Keller HU, Lellouch E. The spectrum of Comet Hale–Bopp (C/1995 01) observed with the Infrared Space Observatory at 2.9 AU from the Sun. Science 1997;275:1904–7.

[2] Hanner MS, Lynch DK, Russell RW. The 8-13 micron spectra of comets and the composition of silicate grains. Astrophys J 1994;425:274–85.

[3] Colangeli L, Mennella V, di Marino C, Rotundi A, Bussoletti E. Simulation of the cometary 10 μm band by means of laboratory results on silicatic grains. Astron Astrophys 1995;293:927–34.

[4] Wooden DH, Harker DE, Woodward CE, Butner HM, Koike C, Witteborn FC, McMurtry CW. Silicate mineralogy of the dust in the inner coma of comet C/1995 01 (Hale–Bopp) pre- and postperihelion. Astrophys J 1999;517:1034–58.

[5] Wooden DH, Woodward CE, Harker DE. Discovery of crystalline silicates in comet C/2001 Q4 (NEAT). Astrophys J Lett 2004;612:L77–L80.

[6] Bradley JP, Keller LP, Snow TP, Hanner MS, Flynn GJ, Gezo JC, Clemett SJ, Brownlee DE, Bowey JE. An infrared spectral match between GEMS and interstellar grains. Science 1999;285:1716–8.

[7] Waelkens C, Waters LBFM, de Graauw MS, Huygen E, Malfait K, Plets H, Vandenbussche B, Beintema DA, Boxhoorn DR, Habing HJ, Heras AM, Kester DJM, Lahuis F, Morris PW, Roelfsema PR, Salama A, Siebenmorgen R, Trams NR, van der Bliek NR, Valentijn EA, Wesselius PR. SWS observations of young main-sequence stars with dusty circumstellar disks. Astron Astrophys 1996;315:L245–8.

[8] Malfait K, Waelkens C, Waters LBFM, Vandenbussche B, Huygen E, de Graauw MS. The spectrum of the young star HD 100546 observed with the Infrared Space Observatory. Astron Astrophys 1998;332:L25–8.

[9] Demyk K, Dartois E, Wiesemeyer H, Jones AP, d'Hendecourt L. Structure and chemical composition of the silicate dust around OH/IR stars. Astron Astrophys 2000;364:170–8.

[10] Molster FJ, Waters LBFM, Tielens AGGM. Crystalline silicate dust around evolved stars. II. The crystalline silicate complexes. Astron Astrophys 2002;382:222–40.

[11] Fulle M. Constraints on the dust size distribution of 46P/Wirtanen from in-situ and ground-based observations. Adv Space Res 1999;24:1087–93.

[12] Moreno F, Lara LM, Muñoz O, López-Moreno JJ, Molina A. Dust in comet 67P/Churyumov–Gerasimenko. Astrophys J 2004;613:1263–9.

[13] Muñoz O, Volten H, de Haan JF, Vassen W, Hovenier JW. Experimental determination of scattering matrices of olivine and Allende meteorite particles. Astron Astrophys 2000;360:777–88.

[14] Konert M, Vandenberghe J. Comparison of laser grain size analysis with pipette and sieve analysis: a solution for the underestimation of the clay fraction. Sedimentology 1997;44:523–35.

[15] Min M, Hovenier JW, de Koter A. Shape effects in scattering and absorption by randomly oriented particles small compared to the wavelength. Astron Astrophys 2003;404:35–46.

[16] Hansen JE, Travis LD. Light scattering in planetary atmospheres. Space Sci Rev 1974;16:527–610.

[17] Volten H, Muñoz O, Hovenier JW, de Haan JF, Vassen W, van der Zande WJ, Waters LBFM. WWW scattering matrix database for small mineral particles at 441.6 and 632.8 nm. JQSRT 2005;90:191–206.

[18] Jäger C, Il'in VB, Henning T, Mutschke H, Fabian D, Semenov D, Voshchinnikov N. A database of optical constants of cosmic dust analogs. JQSRT 2003;79:765–74.

[19] Salisbury JW. Mid-infrared spectroscopy: laboratory data. In: Pieters C, Englert P, editors. Remote geochemical analysis: elemental and mineralogical composition. New York: Cambridge University Press; 1993. p. 79–98.

[20] Hovenier JW. Measuring scattering matrices of small particles at optical wavelengths. In: Mishchenko MI, Hovenier JW, Travis LD, editors. Light scattering by nonspherical particles, theory, measurements and applications. San Diego: Academic Press; 2000. p. 355–65.

[21] Hovenier JW, Volten H, Muñoz O, van der Zande WJ, Waters LBFM. Laboratory study of scattering matrices for randomly oriented particles: potentials, problems, and perspectives. JQSRT 2003;79:741–55.

[22] Hovenier JW, Van der Mee CVM. Basic relationships for matrices describing scattering by small particles. In: Mishchenko MI, Hovenier JW, Travis LD, editors. Light scattering by nonspherical particles, theory, measurements and applications. San Diego: Academic Press; 2000. p. 61–85.

[23] Mishchenko MI, Hovenier JW, Travis LD, editors. Light scattering by nonspherical particles, theory, measurements and applications. San Diego: Academic Press; 2000.

[24] Volten H, Muñoz O, Rol E, de Haan JF, Vassen W, Hovenier JW, Muinonen K, Nousiainen T. Scattering matrices of mineral aerosol particles at 441.6 nm and 632.8 nm. J Geophys Res 2001;106:17375–402.

[25] Chernova GP, Kiselev NN, Jockers K. Polarimetric characteristics of dust particles as observed in 13 comets—Comparisons with asteroids. Icarus 1993;103:144–58.

[26] Rosenbush VK, Rosenbush AE, Dement'ev MS. Comets Okazaki–Levy–Rundenko (1989 19) and Levy (1989 20): polarimetry and stellar occultations. Icarus 1994;108:81–91.

[27] Manset N, Bastien P. Polarimetric observations of comets C/1995 O1 Hale–Bopp and C/1996 B2 Hyakutake. Icarus 2000;145:203–19.

[28] Levasseur-Regourd AC, Hadamcik E. Light scattering by irregular dust particles in the solar system: observations and interpretation by laboratory measurements. JQSRT 2003;79:903–10.